# Chapter 3

# Synthesis and Characterisation of $Sr_2MnO_4$

Part of this chapter is published as 'Gurudeo Nirala, Dharmendra Yadav & Shail Upadhyay; Thermally activated polaron tunnelling conduction mechanism in $Sr_2MnO_4$ synthesized by quenching in ambient atmosphere; *Phys. Scr.* **96**, 045811 (2021).'

## 3.1 Introduction

Mixed electronic and ionic conducting (MEIC) oxide of alkaline earth metals, block-d metals, and lanthanides are used as catalysts, electronic grade ceramics, etc. These oxides have attracted the attention of several groups of researchers who are engaged in synthesizing and characterizing these oxides [179]. The layered perovskite oxide of strontium and manganese, $Sr_2MnO_4$ is one of such oxides which is currently being investigated by several research groups. Mizutani et al [180]. synthesized two allotropic forms of $Sr_2MnO_4$ – (i) a low-temperature α-$Sr_2MnO_4$ phase of undermined structure and (ii) the high-temperature β-$Sr_2MnO_4$ phase, with the $K_2NiF_4$ structure. The β-$Sr_2MnO_4$ phase in literature is simply referred to as $Sr_2MnO_4$. Kriegel et al [181] and Feltz et al [182] using XRD analysis patterns observed that α-$Sr_2MnO_4$ is a mixture of SrO and $Sr_7Mn_4O_{15}$ phases. In 1955 Balz and Plieth [183] confirmed that β-$Sr_2MnO_4$ is iso-structural with the $K_2NiF_4$. An effort has been made to synthesize and stabilize β-$Sr_2MnO_4$ phase at room temperature by using the reducing atmosphere of $N_2$ and/or Ar during synthesis [73]. Single phase powder of β-$Sr_2MnO_4$ had been synthesized by calcining a mixture of SrO and $Sr_7Mn_4O_{15}$ above 1550 °C (for 72 h) with intermediate grinding followed by normal cooling up to room temperature [184]. A critical assessment of the available literature on β-$Sr_2MnO_4$ has shown that its synthesis and stabilization at room temperature are challenging. The requirement of a controlled atmosphere and long calcination time for the synthesis of β-$Sr_2MnO_4$ (commonly known as $Sr_2MnO_4$) increase its cost of production and limit the technological applications in solar cells, cathode materials in solid oxide fuel cells (SOFC), solid oxide electrochemical cells, photo-electrodes, etc. Therefore, in the present work, an effort has been made to develop a simple and inexpensive method for synthesizing $Sr_2MnO_4$. The obtained phase pure powder of $Sr_2MnO_4$ has been characterized using X-ray diffraction (XRD) analysis, Fourier transform infrared (FTIR); UV-visible, X-ray photoelectron (XPS) spectroscopic techniques, and scanning electron microscopic (SEM)

analysis. The electrical conduction behaviour of synthesized $Sr_2MnO_4$ has been studied in the temperature range of 30 - 500°C and a frequency range of 20 Hz – 2 MHz.

## 3.2 Experimental

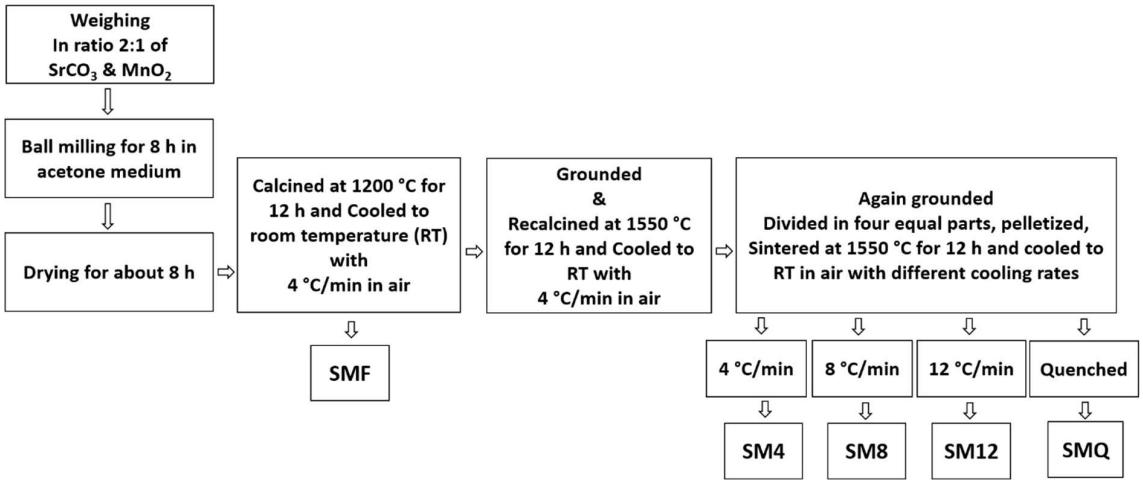


***Figure 3.1. Flow chart of the synthesis of powders and ceramics.***

The layered perovskite oxide $Sr_2MnO_4$ was prepared by the conventional solid-state reaction route. The starting compounds $SrCO_3$ (Sigma-Aldrich, purity ≥ 99.9%) and $MnO_2$ (Sigma-Aldrich, purity ≥ 99%) were taken in the stoichiometric ratio of 2:1 and ball milled in a ball mill (Retsch PM-200, Germany) for 8 hours. The ball-milled mixture thus obtained was calcined at 1200°C for 12 hours in a furnace (Carbolite Gero, HTRH-70/150, UK). The calcined powder thus obtained was further ground using an agate mortar and recalcined at 1500°C for 12 hours. For microstructural and electrical measurements, the pellets of diameter 7-8 mm and thickness 2-3 mm were prepared using a hydraulic press by applying the pressure of 5 kN. All pellets thus prepared were sintered by heating at 1500°C for 12 hours in an electrically heated furnace and cooled to room temperature using controlled cooling rates of 4, 8, and 12° C/min and by direct quenching. The schematic diagram of the entire process is shown in Fig. 3.1. For identification purpose, the powder obtained after calcination at 1200 °C is referred as SMF and

the sintered pellets obtained at the end of four different cooling rates are referred as SM4, SM8, SM12 and SMQ, where 4, 8, 12, and Q designate the cooling rates and quenching, respectively.

The X-ray diffraction (XRD) patterns of powder samples obtained at different stages was recorded at room temperature using an X-ray diffractometer (Rigaku Miniflex II Desktop, Japan) equipped with $Cu\ K_\alpha$ radiation system. The FTIR spectra of two representative samples SM4 and SMQ were recorded using a FITR spectrometer (JASCO FT/IR-4600, Japan) in the attenuated total reflection (ATR) mode in the wave number range of 400 - 4000 $cm^{-1}$. The XPS analysis of the sample SMQ was performed using an X-ray photo-electron spectrometer (Thermo Fisher Scientific K-Alpha, USA) at the pressure of $5x10^{-11}$ Torr. The UV-visible spectra of sample SMQ were recorded using UV-Visible spectrophotometer (JASCO V-770, Japan) in the wavelength range of 500-1500 nm. The morphological fingerprints of sintered pellets were recorded using a field emission Scanning Electron Microscope (Nova Nano SEM 450, USA). For measuring the electrical properties of sintered pellets, the two flat surfaces (end surfaces) of each pellet were polished using emery paper of different grades and then coated with a thin and uniform layer of high temperature silver paste. The resistances and capacitances of the sample SMQ ($Sr_2MnO_4$) were measured as a function of the frequency in the range of 0.02–2 MHz and temperature in the range of 30-500 $^oC$ using an inductance-capacitance-resistance (LCR) meter (Agilent E-4980, USA).

## 3.3 Results and Discussions

The results of phase analysis, structural characterization, and electrical properties measurement are presented and discussed in the following pages.

### 3.3.1 Phase Analysis and Structural Characterization

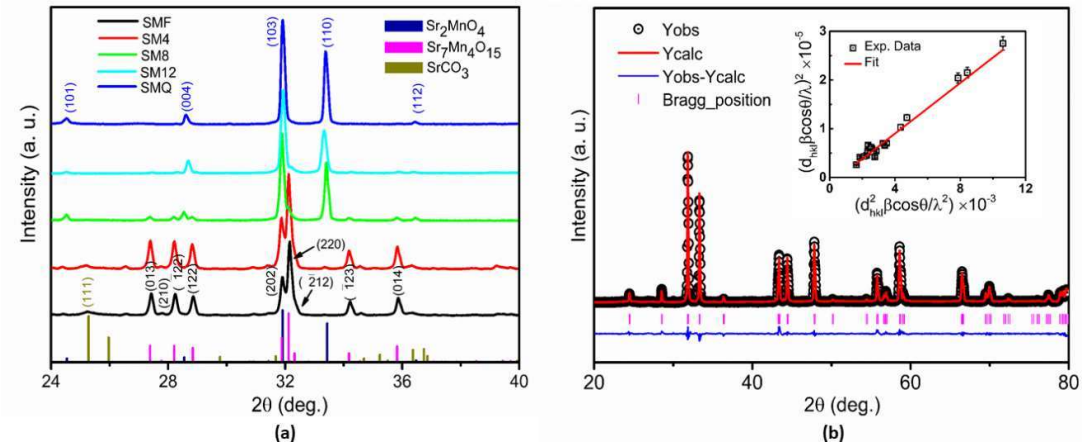


***Figure 3.2. (a) XRD pattern of the samples, (b) Rietveld refinement of XRD data, and SSP plot (inset) of the sample SMQ ($Sr_2MnO_4$).***

The room-temperature X-ray diffraction (XRD) patterns of all the samples was recorded in the 2θ range of 20 to 80° with step size of 0.02° and scan rate of 4°/min. It has been reported that intense XRD peaks of the reactants, product, and impurity phases lie in the range of 24° < 2θ < 40°. Therefore, for the sake of clarity, in Fig. 3.2(a) the XRD patterns of various samples are shown in the 24° < 2θ < 40° range only. The XRD peaks were matched and indexed using the Crystallography Open Database (COD) for $Sr_2MnO_4$ (1008125), $Sr_7Mn_4O_{15}$ (1526876) and $SrCO_3$ (5000093) phases. The peak positions and their relative intensities for respective CODs are shown in different colours. The XRD patterns of samples SMF, SM4, and SM8 match well with the XRD patterns of phase $Sr_7Mn_4O_{15}$. As mentioned in the experimental section, the compounds $SrCO_3$ and $MnO_2$ were taken in the molar ratio of 2:1. Therefore, in samples SMF, SM4, and SM8, the presence of some amount of un-reacted SrO is expected according to Eqn. (3.1):

$$8SrCO_3 + 4MnO_2 \rightarrow Sr_7Mn_4O_{15} + SrO + 8CO_2 \uparrow \rightarrow 4Sr_2MnO_4 \qquad (3.1)$$

The product SrO may react with $CO_2$ and stabilize as $SrCO_3$. The XRD patterns of SMF and SM4 exhibit a broad but weak intensity peak corresponding to $SrCO_3$ at 25.3°. A small

peak at 33.4° in the patterns of SM4 does not match with the XRD patterns of $Sr_7Mn_4O_{15}$, but it matches well with the second intense peak of $Sr_2MnO_4$. The most intense peak of $Sr_2MnO_4$ at 31.9° overlaps with the second intense peak of $Sr_7Mn_4O_{15}$. The peak at 31.9° in the XRD patterns of sample SM4 may have a small contribution from the most intense peak of $Sr_2MnO_4$. Hence, the presence of a small amount of $Sr_2MnO_4$ phase along with $Sr_7Mn_4O_{15}$ phase in the sample SM4 cannot be denied. Similar conclusions could also be drawn from the XRD patterns of samples SM8 and SM12. The XRD patterns of SMQ exhibits peaks corresponding to only $Sr_2MnO_4$ phase. Thus, it can be inferred that samples SM4, SM8, and SM12 constitute mixed-phases (both $Sr_7Mn_4O_{15}$ and $Sr_2MnO_4$) whereas in the sample SMQ only $Sr_2MnO_4$ phase is present.

The percentage (%) of the secondary phase in the powder of any sample can be calculated using the formula: $\varphi = I_p/(I_p + 0.8 * I_s)$, where $I_p$ is the maximum intensity of the primary phase and $I_s$ is the maximum intensity of the secondary phase [185]. The percentage of two phases $Sr_7Mn_4O_7$ and $Sr_2MnO_4$ in the powder of different samples was calculated and are given in Table 3.1. From this table, it is observed that as the cooling rate increases the percentage (%) of $Sr_2MnO_4$ phase in the synthesized powder also increases.

**Table 3.1. Effect of cooling rate on the percentage (%) of two major phases in the synthesized powders.**

| Sample Code | Percentage (%) | |
|---|---|---|
| | $Sr_7Mn_4O_{15}$ | $Sr_2MnO_4$ |
| **SM4** | 93.6 | 6.4 |
| **SM8** | 13.6 | 86.3 |
| **SM12** | 10.1 | 89.9 |
| **SMQ** | 0 | 100 |

Structural parameters of sample SMQ (comprising the only $Sr_2MnO_4$ phase) were obtained with the help of Rietveld refinement using the FullProf Suite software package. The structural refinement was carried out by considering the tetragonal structure and space group I4/mmm for $Sr_2MnO_4$. The calculated XRD patterns obtained after the final refinement is shown in Fig. 3.2(b). The good match between the observed and calculated patterns indicates that the quenching has not induced any major structural ambiguity. The lattice parameters, selected bond lengths along with reliability factors of Rietveld refinement are listed in Table 3.2. For comparison, the values of structural parameters as reported in the COD file of $Sr_2MnO_4$ are also given in Table 3.2. It is observed that the refined values of the structural parameters are in good agreement with the values given in the COD file of $Sr_2MnO_4$ [186].

The crystallite size of the powder of SMQ (the $Sr_2MnO_4$ phase) was calculated by the Size-Strain Plot (SSP) method. As per the SSP method, the inter-planar spacing and the micro-strain are related according to Eqn. (3.2) [187],

$$\left(\frac{d_{hk}\,\beta cos\theta}{\lambda}\right)^2 = \frac{k\lambda}{D}\left(\frac{d_{hkl}^2\beta cos\theta}{\lambda^2}\right) + \left(\frac{\varepsilon}{2}\right)^2 \qquad (3.2)$$

where, $d_{hkl}$ is the interplanar spacing corresponding to the plane $(hkl)$, $D$ is the crystallite size, $k$ is the constant = 3/4 for spherical particles, λ is the wavelength of X-ray, $\beta$ is the full width at half maximum (FWHM) of diffraction peak, $\theta$ is the Bragg's diffraction angle, and $\varepsilon$ is the average strain generated in the lattice. The plot of $\left(\frac{d_{hk}\,\beta cos\theta}{\lambda}\right)^2$ vs. $\left(\frac{d_{hkl}^2\beta cos\theta}{\lambda^2}\right)$ for the sample, SMQ is shown as the inset in Fig. 3.2(b). By the linear regression of the experimental data points, the value of crystalline size and lattice strain was calculated as given in Table 3.2. The order of calculated strain matches with the order of strain reported for other undoped $A_2BO_4$ compounds [188]. This indicates that the quenching has not produced any severe strain in the lattice of $Sr_2MnO_4$, which is likely to lead to the long-time stability of the structure in the

synthesized sample SMQ. The stability of the $Sr_2MnO_4$ phase in the sample SMQ was experimentally checked by recording the XRD patterns of the powder after about six months and it was found that the XRD patterns of fresh and 6-month-old samples were identical. This confirmed the prolonged stability of $Sr_2MnO_4$ phase and ruled out any possibility of decomposition into reactants $SrCO_3$ and $MnO_2$ or even conversion into the allotropic phase $Sr_7Mn_4O_{15}$ for that matter.

**Table 3.2. Structural parameters and reliability factors for sample SMQ ($Sr_2MnO_4$) obtained by Rietveld refinement of the XRD patterns.**

| Structural Parameters | | $Sr_2MnO_4$ (SMQ) | COD file [186] |
|---|---|---|---|
| Lattice Parameters | a = b | 3.795 Å | 3.787 Å |
| | C | 12.500 Å | 12.496 Å |
| Atomic coordinates | Sr | (0, 0, 0.357) | (0, 0, 0.356) |
| | Mn | (0, 0, 0) | (0, 0, 0) |
| | O1 | (0, 0.5, 0) | (0, 0.5, 0) |
| | O2 | (0, 0, 0.161) | (0, 0, 0.157) |
| Bond Lengths | Mn-O1 | 1.897 Å | 1.893 Å |
| | Mn-O2 | 2.018 Å | 1.962 Å |
| | Sr-O1 | 2.607 Å | 2.612 Å |
| | Sr-O2 | 2.693 Å | 2.486 Å |
| | Mn-O1/Mn-O2 | 0.94 | 0.96 |
| Reliability Factors | $R_p$ | 37.7 | |
| | $R_{wp}$ | 32.8 | |
| | $R_{exp}$ | 12.97 | |
| | $\chi^2$ | 4.01 | |
| | $S=R_p/R_{wp}$ | 1.14 | |
| Crystallite Size | D | 41.71 nm | |
| Strain | Ɛ | 3.66 $\times 10^{-3}$ | |

### 3.3.2 FTIR Spectroscopic Studies

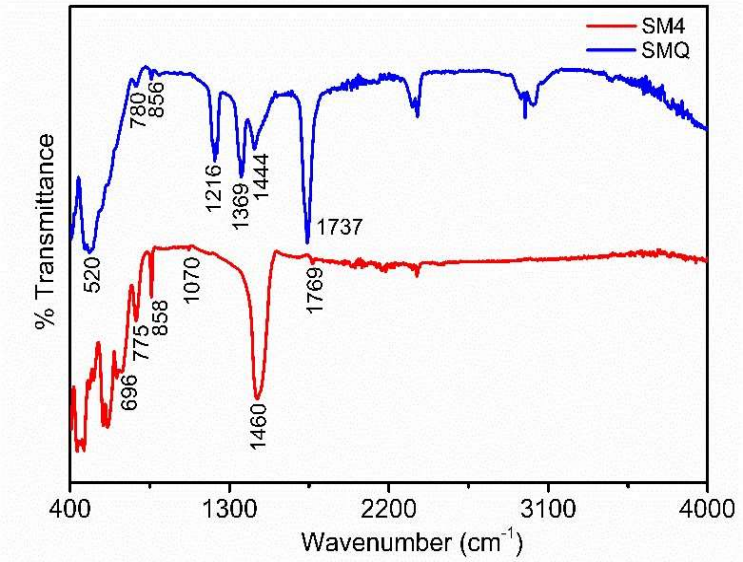


***Figure 3.3. FTIR spectra of samples SM4 and SMQ ($Sr_2MnO_4$).***

As the prepared sample of SMF contains $SrCO_3$ as an impurity, it may also be present in all four sintered samples. The FTIR spectroscopy is a very sensitive technique to detect the presence of alkaline earth carbonates [189]. Hence, the FTIR spectra of all the samples were recorded in the wave number range of 400-4000 $cm^{-1}$ with step size of 1 $cm^{-1}$. The FTIR spectra of two representative samples SM4 and SMQ are shown in Fig. 3.3. In the FTIR spectrum of SMQ strong broadband at 520 $cm^{-1}$ is observed which corresponds to the Mn-O-Mn stretching vibration in $MnO_6$ octahedron [190]. Besides this characteristic band, a few weak bands at 780 $cm^{-1}$ (C-H bending vibration), 856 $cm^{-1}$ (out of plane bending vibration of $SrCO_3$), 1216 $cm^{-1}$ (C-O stretching vibration), 1369 $cm^{-1}$ (C-H stretching vibration), 1444 $cm^{-1}$ (asymmetric stretching vibration of C-O bonds) and 1737 $cm^{-1}$ (bending vibration of -OH bond) are also seen in the spectrum. On the other hand, in the FTIR spectrum of SM4, several extra bands at 696 $cm^{-1}$ (in-plane bending vibration of $SrCO_3$), 775 $cm^{-1}$ (C-H bending vibration), 858 $cm^{-1}$ (out of plane bending vibration of $SrCO_3$), 1070 $cm^{-1}$ (symmetric stretching vibration of C-O bonds), 1460 $cm^{-1}$ (asymmetric stretching vibration of C-O bonds) and 1769 $cm^{-1}$ (bending

vibration of -OH bond)[191,192][191,192] are observed [191,192]. A comparison of the FTIR spectra of SM4 and SMQ has indicated that in the spectrum of SMQ bands corresponding only to the asymmetric vibrations of C-O are present whereas in the spectrum of SM4 bands corresponding to both symmetric and asymmetric vibrations of C-O are present. The presence of bands corresponding to asymmetric vibrations of C-O only in the spectrum of the sample SMQ suggests that the observed vibrations are due to the adsorbed $CO_2$ molecules on the surface of the particles and not due to the un-reacted $SrCO_3$.

### 3.3.3 Microstructural Studies

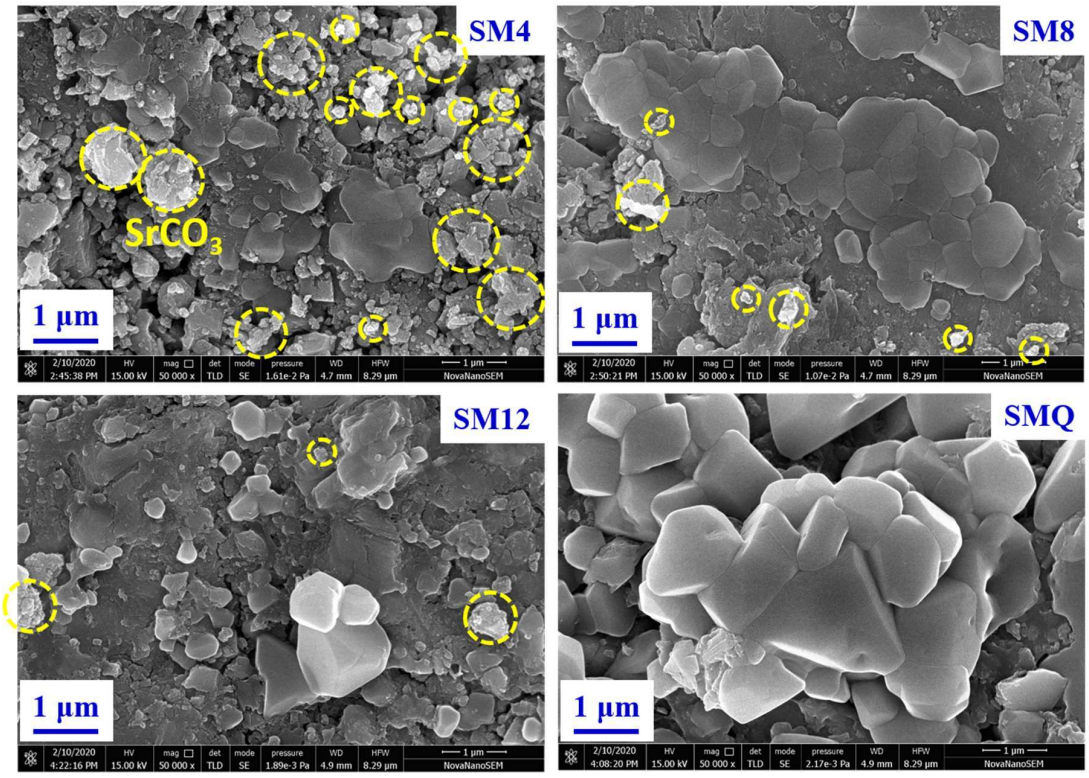


***Figure 3.4. SEM micrographs of a sintered pellet of samples.***

To study the effect of cooling rate on the microstructure, the morphology of polished surfaces of the sintered pellets of the prepared samples was studied using respective scanning electron micro-photographs (SEM). Fig. 3.4 shows the SEM micrographs of the sintered samples of SM4, SM8, SM12, and SMQ. The micrographs of samples SM4, SM8, and SM12

are heterogeneous and contain grains of different shapes and sizes. On the other hand, the micrograph of the sample SMQ is homogenous. A noticeable change in the microstructure with an increase in the cooling rate is seen. Moreover, it is observed that on increasing the cooling rate, the fraction of large size grains increases. Thus, it can be inferred that due to the slow cooling rate, some amount of $Sr_2MnO_4$ phase decomposes into $Sr_7Mn_4O_{15}$ and SrO ($SrCO_3$). This is because below 1350 $^oC$ the stability of $Sr_7Mn_4O_{14}$ phase is higher than that of $Sr_2MnO_4$ phase [165]. As the cooling rate increases the chance of decomposition of $Sr_2MnO_4$ decreases, which explains the presence of only $Sr_2MnO_4$ phase in the quenched sample SMQ. The micrograph of the sample SMQ ($Sr_2MnO_4$) has well developed cuboidal shape grains separated by well-defined grain boundaries, a typical characteristic feature of a polycrystalline material. As per the objective of this work, in the succeeding sections, experimental results of only sample SMQ ($Sr_2MnO_4$) have been described.

### 3.3.4 UV-Visible Spectroscopic Studies

The UV-visible spectrum of the sample SMQ was recorded in the wavelength range of 200-1700 nm with step size of 1 nm. The absorption spectrum of the sample SMQ is shown as the inset in Fig. 3.5(a). About 90% absorbance in the entire visible region has been observed. The spectrum shows a sharp absorption edge close to the band-gap. To determine the band-gap, absorption data has been plotted according to the Tauc's equation for direct bandgap, given by [193]:

$$(\alpha h\nu)^2 = B(E - E_g) \qquad (3.3)$$

where $\alpha$ is the absorption coefficient, $h$ is the Planck's constant, $\nu$ is the frequency of the incident photon, $E_g$ is the band-gap energy, and $B$ is the energy independent constant. Tauc's plot is shown in Fig. 3.5(a). The optical band-gap has been determined from the intercept of the tangent to the curve of the plot between $(\alpha h\nu)^2$ vs. photon energy ($h\nu$) on the x-axis i. e.

for $(\alpha h\nu)^2 = 0$. The computed value of the band-gap of the sample SMQ ($Sr_2MnO_4$) is found to be 1.15 eV which is consistent with the values obtained from the theoretical calculation using different models [194,195].

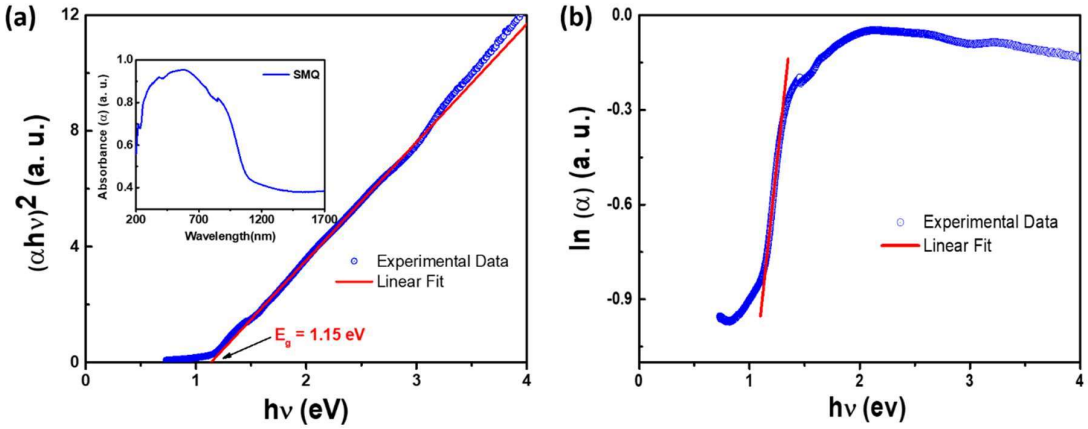


***Figure 3.5. (a) Tauc's plot for sample SMQ ($Sr_2MnO_4$). The UV-visible absorption spectrum is shown in the inset. (b) ln (α) versus hν plot for determining Urbach tail width.***

The reduction of Mn ions from $Mn^{4+}$ to $Mn^{3+}$ oxidation state generates defect centers in the crystal due to mismatch in ionic radius as well as charge compensation mechanism. The defects introduce a strong potential gradient in the host matrix, which causes the quantum mechanical penetration of the localized states into the forbidden band-gap. The degree of disorder in the crystal introduced due to defect centers can be estimated by determining the Urbach tail width. In optical absorption spectra, near band edges have an exponential part called exponential tail (Urbach tail). In the energy range $E < E_g$, an exponential dependence of the absorption coefficient (α) on photon energy (hν) (Urbach tail) is expressed as [196]:

$$\alpha = \alpha_0 \, exp\left(\frac{h\nu}{E_u}\right) \qquad (3.4)$$

where $\alpha_0$ is a constant, $E_u$ is the Urbach tail width estimated from the reciprocal slope of the linear part of $ln\ \alpha$ versus $h\nu$ plot. From Fig. 3.5(b), we find the value of $E_u$ for the sample SMQ ($Sr_2MnO_4$) is 306 meV. Which is fairly high [196,197], indicates a higher concentration

of defect centers in the synthesized sample SMQ. It is consistent with our XPS studies. Which has resulted as about 34 % Mn ions in $Mn^{3+}$ and remaining 64 % in $Mn^{4+}$ oxidation state.

### 3.3.5 XPS Analysis

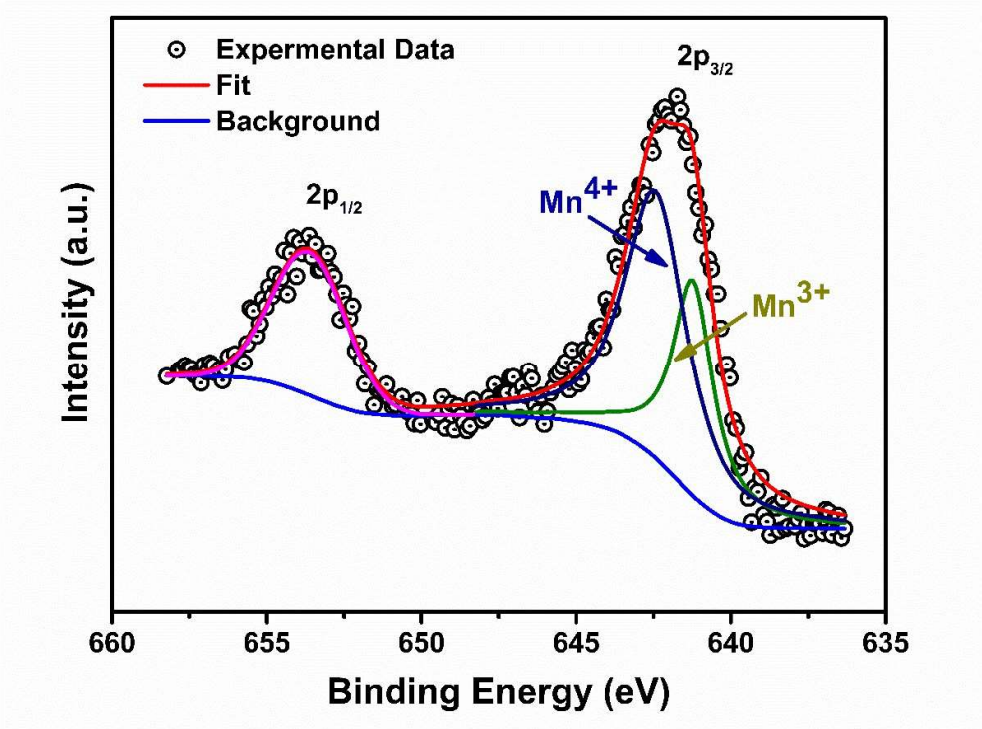


***Figure 3.6. XPS spectra of Mn 2p present in the sample SMQ ($Sr_2MnO_4$). Symbols represent the recoded spectrum and the solid line represents the fit and background.***

To know the valence state of Mn ions, present in the sample SMQ ($Sr_2MnO_4$), the x-ray photoelectron spectroscopy (XPS) technique was employed. Fig. 3.6 depicts the Mn-2p core-level spectrum. The two distinct peaks observed at 654 and 642 eV are attributed to $2p_{1/2}$ and the $2p_{3/2}$ states of Mn, respectively. The asymmetrical nature of the Mn $2p_{3/2}$ peak leads to the deconvolution of the peak into two pairs of peaks. The de-convoluted peaks centered at 641.2 and 642.5 eV correspond to the $Mn^{3+}$ and $Mn^{4+}$ states of Mn ions, respectively [198]. This result indicates that in the sample SMQ ($Sr_2MnO_4$), Mn ions exist in both $Mn^{4+}$ and $Mn^{3+}$ valence states. Quantitative estimation by the integrated area of the peaks showed the concentration of $Mn^{4+}$ and $Mn^{3+}$ as around 64 and 36%, respectively. Similar values of the

binding energies of oxygen vacancy and the adsorbed oxygen complicate the estimation of the concentration of oxygen vacancies using XPS [198,199]. The presence of some of the Mn ions in the $Mn^{3+}$ valence state indirectly supports the existence of the oxygen vacancies in the synthesized SMQ ($Sr_2MnO_4$) sample.

## 3.4 Electrical Studies

The electrical properties of the sample SMQ ($Sr_2MnO_4$) have been studied at different temperatures and frequencies. The results obtained are presented and discussed in the following sections.

### 3.4.1 AC conductivity

To understand the conduction mechanism of $Sr_2MnO_4$(SMQ), frequency-dependent conductivity values in the temperature range of 30 to 500 °C were recorded at an interval of 10 °C. The variation of the log of total conductivity ($\sigma_{tol.}$) versus the log of frequency (f) at different temperatures is shown in Fig. 3.7. In each case a plateau region of constant conductivity (DC conductivity) below a certain frequency, and above it, a linear increase in the conductivity with a frequency is seen. Further, it is noticed that the DC conductivity and frequency-independent region (the plateau region) increases with increasing temperature. The increase in the DC conductivity with an increase in temperature reflects the semiconducting behavior of $Sr_2MnO_4$ (SMQ). An increase in the conductivity with increasing frequency may arise due to the presence of defects and space charge regions in the sample. For the materials containing defects the total conductivity is generally expressed as:

$$\sigma_{tot} = \sigma_{dc} + \sigma_{ac} \qquad (3.5)$$

The AC conductivity ($\sigma_{ac}$) is often described by the Jonscher′s Power Law (JPL) written as [200]:

$$\sigma_{AC}(\omega, T) = A(\omega)^n \qquad (3.6)$$

where $A$ is a constant, $\omega$ $(= 2\pi f)$ is the angular frequency and $n$ is the frequency exponent that lies between $0 < n < 1$.

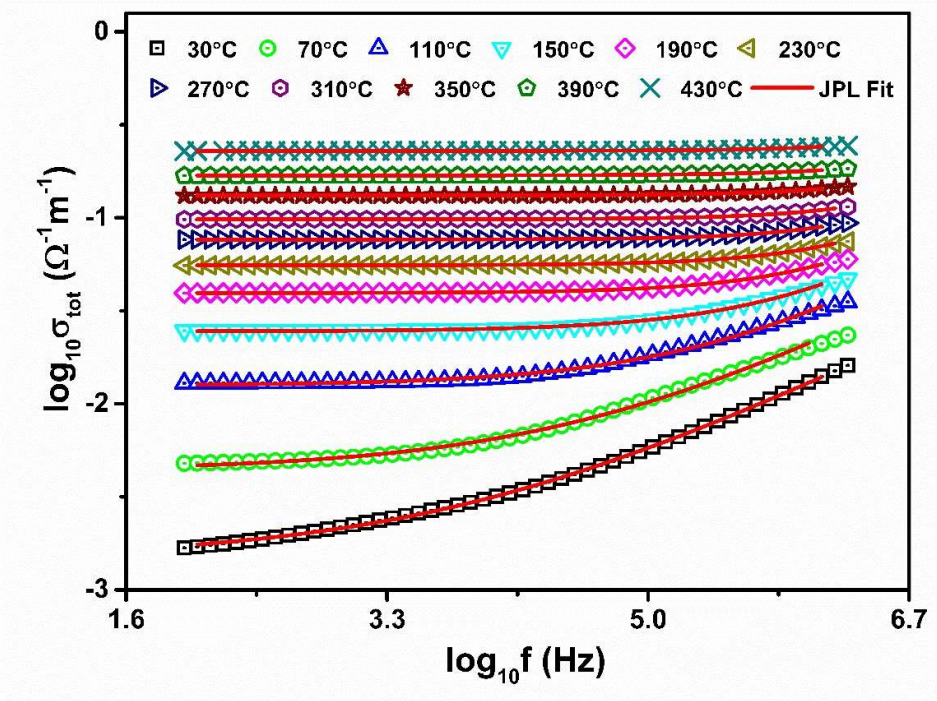


***Figure 3.7. Conductivity spectra of the sample SMQ ($Sr_2MnO_4$) at different temperatures. Symbols represent the experimental data points and the solid lines represent the theoretical JPL fitting.***

Eqn. (3.5) can be rewritten as:

$$\sigma_{tot} = \sigma_{dc}\left[1 + \left(\frac{f}{f_h}\right)^n\right] \qquad (3.7)$$

where, $f_h = \left(\frac{\sigma_{dc}}{A}\right)^{\frac{1}{n}}$

The term $f_h$ is known as the hopping frequency, which is the onset of conductivity dispersion in the conductivity spectra. Eqn. (3.7) is known as the Almond and West representation of Jonscher's power law. Fig. 3.7 shows the non-linear curve fitting of the experimental data points obtained at different temperatures to Eqn. (3.7). The solid lines represent the fitted

curves and symbols represent the corresponding experimental data points. Through this curve fitting, values of DC conductivity ($\sigma_{dc}$), hopping frequency ($f_h$) and frequency exponent ($n$) at different temperatures were estimated.

The log $\sigma_{dc}$ versus the inverse of temperature (1000/T) plot shown in Fig. 3.8 was used to understand the mechanism of DC conduction in the sample SMQ ($Sr_2MnO_4$). In this plot, three distinct linear regions (I, II, and III) with different slopes are seen. The observed linear nature of log $\sigma_{dc}$ vs. 1000/T plot in each region suggests that the conductivity follows the Arrhenius type relation given as:

$$\sigma_{dc} = \sigma_o \exp\left(-\frac{E_a}{kT}\right) \qquad (3.8)$$

where, $\sigma_o$, $E_a$, $k$ and $T$ are the pre-exponential factor, activation energy, Boltzmann constant, and absolute temperature, respectively. The activation energy of the conduction in each region was determined by fitting the conductivity data to the above Arrhenius relation. The estimated values of activation energy for Region I (30-150$^o$C), Region II (150-340$^o$C) and Region III (340-500$^o$C) are 0.29, 0.18 and 0.36 eV, respectively. The different value of the activation energy for each temperature region suggests a different conduction mechanism for each region. The values of activation energies of the sample SMQ ($Sr_2MnO_4$) for all three regions are less than half the band gap energy $E_g$ (= 1.15eV calculated using Tauc's plot) which signifies separation between Fermi level and conduction band. This result rules out the possibility of intrinsic conduction in any region and suggests extrinsic conduction due to the presence of defects. It is worthwhile to mention here that the sample SMQ ($Sr_2MnO_4$) was prepared by quenching it in air from the sintering temperature 1500 $^o$C to the room temperature. During prolong sintering at higher temperatures, loss of oxygen occurs according to the reactions given below [201]:

$$O_o^{\times} \leftrightarrow \frac{1}{2}O_2(g) + V_o^{\times} \qquad (3.9)$$

$$V_o^{\times} \rightarrow V_o^{\bullet} + e' \qquad (3.10)$$

$$V_o^{\bullet} \rightarrow V_o^{\bullet\bullet} + e' \qquad (3.11)$$

where all the species are written according to the Kroger–Vink notation of defects. The oxygen lost during sintering is regained (re-oxidation) by the sample during cooling from the sintering temperature to the room temperature. Due to continuously decreasing temperature (cooling) of the sample, diffusion of oxygen within the pellets is reduced hence the re-oxidation is restricted only to surfaces and grain boundaries leaving the grains oxygen-deficient as per Eqn. (3.9). The sample SMQ ($Sr_2MnO_4$) has been synthesized by quenching (very fast cooling rate) from the sintering temperature (1500°C) to room temperature in air, hence a higher concentration of oxygen vacancies in the bulk of the sample is presumed. When a neutral oxygen vacancy ($V_o^{\times}$) is singly ionized ($V_o^{\bullet}$) (Eqn. (3.10)) the released electron can localize on $Mn^{4+}$ ion in the neighbor of the oxygen vacancy, as a defect/polaron ($Mn_{Mn^{4+}}^{3+})'$. Analysis of the XPS spectra of Mn-2p (Fig. 3.6) has confirmed the presence of Mn ions in both the valence states $Mn^{3+}$ and $Mn^{4+}$. The presence of $Mn^{3+}$ distorts the lattice of $Sr_2MnO_4$. The ionic radius in the 6-coordination number state of $Mn^{3+}$ is 0.64 nm which is larger than the ionic radius 0.53 nm of the $Mn^{4+}$ in the same coordination number state. Hence, the length of the $Mn^{3+}$-O bond is slightly elongated as compared to the equilibrium length of the $Mn^{4+}$-O bond. A polaron is a defect in which an electronic carrier gets trapped at a given site because of the displacement of adjacent ions. In such a case, the polaron (carrier plus distortion) then migrates by an activated hopping/tunnelling mechanism. Generally, the formation of polaron occurs in the materials whose conduction electrons belong to the incomplete inner $d-$ or $f-$ shells, due to small electrons overlap and tend to form extremely narrow bands. In many transitions, metals-based

oxides including ferrites and $CeO_2$ polarons are the majority carriers and polaronic conduction takes place [202–205]. In $Sr_2MnO_4$ also conduction band belongs to the incomplete $d$-shells of Mn, hence the possibility of formation of polarons in the sample is high. And hence, conduction in the sample of SMQ ($Sr_2MnO_4$) can take place by the migration of polarons as well as oxygen vacancies. It is also possible that at lower temperatures oxygen vacancies are in the singly ionized state ($V_o^{\bullet}$) in the same unit cell in which defect $(Mn_{Mn^{4+}}^{3+})'$ is present. These defects can move together locally from one octahedron to another octahedron. With the increase in temperature singly ionized oxygen vacancies get ionized to doubly ionized vacancies (Eqn. (3.11)) and electron released during this process may get captured by some of the $Mn^{4+}$ ions to get converted into $Mn^{3+}$ ions leading to the increase in the number of polarons $(Mn_{Mn^{4+}}^{3+})'$ defects.

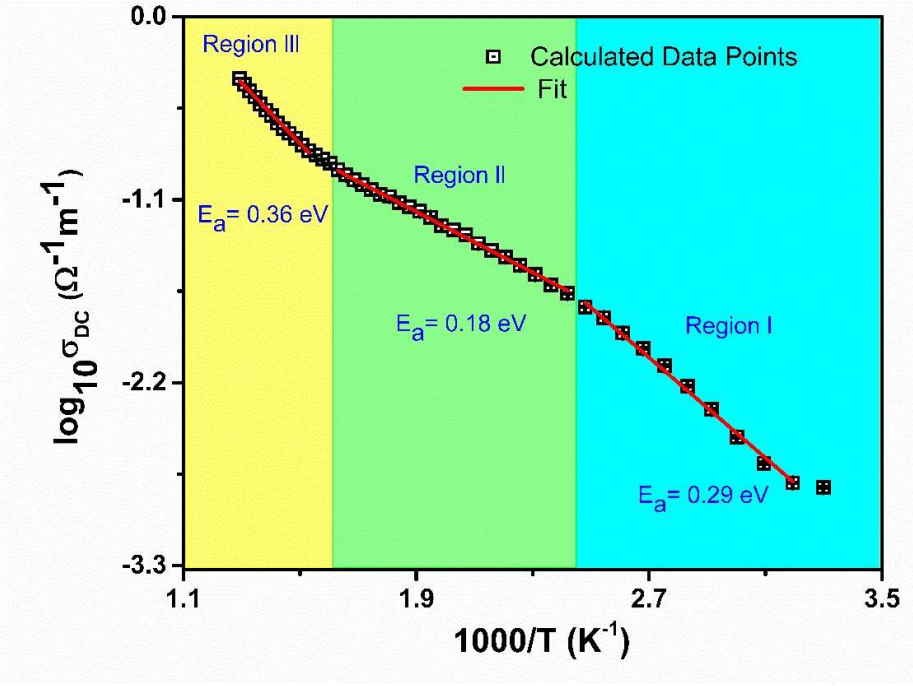


***Figure 3.8. Arrhenius representation of DC conductivity for sample SMQ ($Sr_2MnO_4$).***

Generally, the value of the activation energy for the higher temperature region is higher than for the lower temperature region. But in the present case, the value of the activation energy for region II (160-350°C) is lower as compared to that for the region I (35-160°C). This can be

explained by assuming that at lower temperatures (in the region I) polaron and oxygen vacancy are bounded together and are moving as a single charge carrier within the grains. Micrograph of the synthesized $Sr_2MnO_4$ (Fig. 3.4) shows well-developed grains separated by grain boundaries i.e. a polycrystalline nature. Further, due to quenching, re-oxidation could be limited to the grain boundaries leaving the gains oxygen deficient. The re-oxidation of grain boundaries makes grain boundaries more insulating as compared to grains. The polarons and oxygen vacancies reaching the insulating grain boundaries would pile up due to the higher resistance of the grain boundaries. It is possible that in the temperature region II, on account of the lower thermal energy, some of the polarons may manage to tunnel (the quantum mechanical effect) through the barrier imposed by the grain boundaries leaving behind oxygen vacancies and other polarons. On further increase in the temperature (in region III) oxygen vacancies also join polarons, and once again start to move as a single particle. Theoretical results have shown that in $CeO_{2-\delta}$, oxygen vacancies are strongly attracted to polarons (localized electrons), forming associates between them. The migration energy of an oxygen vacancy in such an association is substantially lower as compared to the un-associated case due to the simultaneous positional rearrangement of the localized electrons during the ionic jump process [206]. Estimated values of activation energy for regions I and II are in agreement with the values reported for $Sr_{2-x}La_xMnO_{4+\delta}$ [207]. The value of activation energy (0.36 eV) for region III is the same as that reported for the oxygen-deficient $Ca_2MnO_{4-\delta}$ [208]. Using the atomic computer simulation of oxide ion conduction in tetragonal $La_2NiO_4$ Cleave *et al.* have shown that activation energy for oxide ion migration within the ab-plane via apical sites is 0.35 eV [82]. Further, it is also reported that the activation energies required for the migration of singly and doubly ionized oxygen vacancies in perovskite oxides fall in the range of 0.3-0.6 eV and 0.7-1.2 eV, respectively [209–212]. The value of the activation energy obtained for the region III (0.36 eV) indicates the possibility of migration of singly ionized oxygen vacancies in the

prepared sample SMQ ($Sr_2MnO_4$). For the evidence of conduction via migration of singly oxygen in the synthesized $Sr_2MnO_4$, measurement of conductivity with respect to oxygen partial pressure is needed.

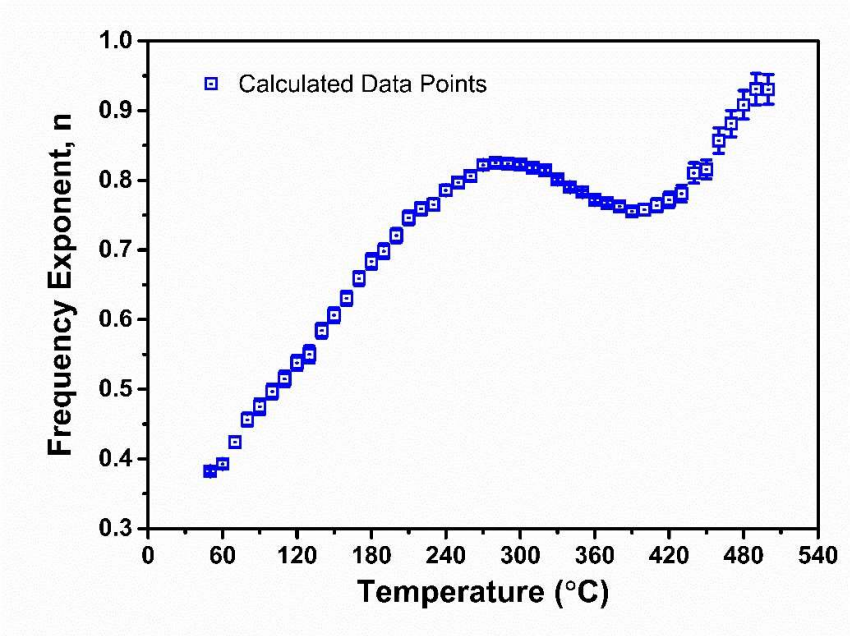


***Figure 3.9. Variation of frequency exponent n with temperature for the sample SMQ ($Sr_2MnO_4$).***

Several theoretical models are available in the literature for explaining the AC conduction behavior of ceramic oxides and glasses. It is well known that if the exponent, $n$ of the frequency shows an increasing trend with temperature then the conduction mechanism is attributed to the non-overlapping small polaron tunnelling (NSPT). In contrast to this, according to the overlapping large polaron tunnelling (OLPT) mechanism, the value of $n$ decreases with temperature reaches a minimum value and then further increases. The quantum mechanical tunnelling (QMT) of polarons is characterized by a temperature independent value of $n$. On the other hand, a decreasing value of $n$ with temperature corresponds to the correlated barrier hopping phenomena (CBH) [213]. The variation of frequency exponent, $n$ with frequency/temperature has been used by earlier workers to know the exact mechanism of conduction by polarons. The variation of exponent, $n$ obtained from the fitting of the

conductivity-temperature data using Eqn. (3.7), with temperature for the sample SMQ ($Sr_2MnO_4$) is shown in Fig. 3.9. It is observed that the value of $n$ initially increases with increasing temperature up to 270 °C, thereafter it begins to decrease and attains a minimum value, and after that once again starts increasing with increasing temperature. Based on this result as well as the results of various theoretical models, the mechanism for conduction in the temperature range of 30-270°C is attributed to tunnelling of small polarons and in the temperature range of 270-500°C to the tunnelling of overlapping-large polarons. Nature (whether small or large) of polaron is governed by two fundamental interaction potentials. The first one is long-range Coulomb potential (LRCP) between an excess charge and lattice ions, and the second is the short-range deformation potential (SRDP) that relates electronic energy to strain. For large polaron, LRCP dominates, and coherence length ($L_{coh}$) is larger than the unit cell dimension (a). On the other hand, when SRDP dominates, $L_{coh}$ is smaller than the unit cell dimension (a) and the result is a small polaron. Further, a large polaron is delocalized over multiple unit cells and its transport is band-like that is $d\mu/dT < 0$ means carrier mobility ($\mu$) decreasing with increasing temperature (T). Whereas a small polaron is localized to a unit cell and its transport occurs via thermally activated hopping, that is, $d\mu/dT > 0$ [214]. Therefore, to confirm the change in the conduction mechanism from small polaron tunnelling to large polaron tunnelling, the study of mobility ($\mu$) as a function of temperature is required.

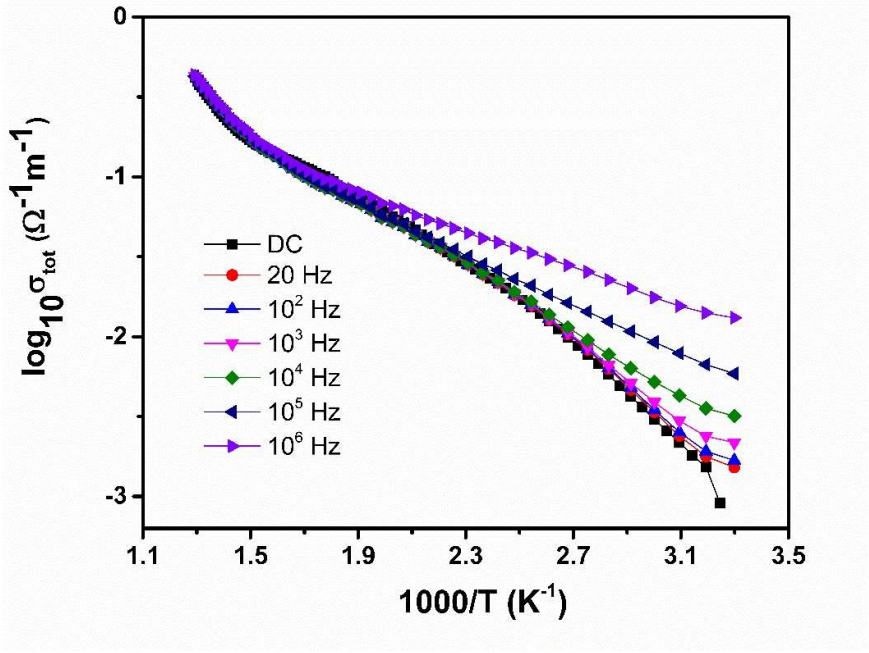


***Figure 3.10. Total conductivity of sample SMQ ($Sr_2MnO_4$) at different frequencies.***

To have a proper understanding of the change in the domain of the conducting species, the total conductivity is plotted against the inverse of absolute temperature at a few selected frequencies in Fig. 3.10. At lower temperatures (below 270°C) a wide dispersion in the conductivity is observed. On the other hand, at higher temperatures (above 270°C), the dispersion in the conductivity reduces drastically and the curves for different frequencies appear to merge with the DC conductivity curve. The dispersion in conductivity at lower temperatures (below 270°C) may arise due to the difference in the number of charge carriers participating in conduction at different frequencies. As the temperature increases, the charge carriers bounded with either lattice ions or with the defects become free via the thermally activated process and dispersion in conductivity with frequency decreases gradually and vanishes at higher temperatures (that is it becomes a function of temperature only). Thus, it is confirmed that in the synthesized sample SMQ ($Sr_2MnO_4$), there is a change in the domain of the migration of charged species from the short-range to a long-range domain.

For many ion-conducting materials, it has been observed that the AC conductivity at different temperatures can be scaled into a single curve. To further confirm the change in the conduction range, the conductivity values of the sample SMQ were scaled. The existence of such a master curve is referred to as the "time-temperature superposition principle (TTPS)". In the past few years, different scaling models for the AC conductivity have been proposed [215–217]. Among these models, Ghosh's scaling model has emerged as a more realistic model. In this model DC conductivity ($\sigma_{dc}$) and hopping frequency ($f_h$ ) are used as scaling parameters according to the relation given below [218]:

$$\frac{\sigma_{tot}(f)}{\sigma_{dc}} = \mathcal{F}\left(\frac{f}{f_h}\right) \qquad (3.12)$$

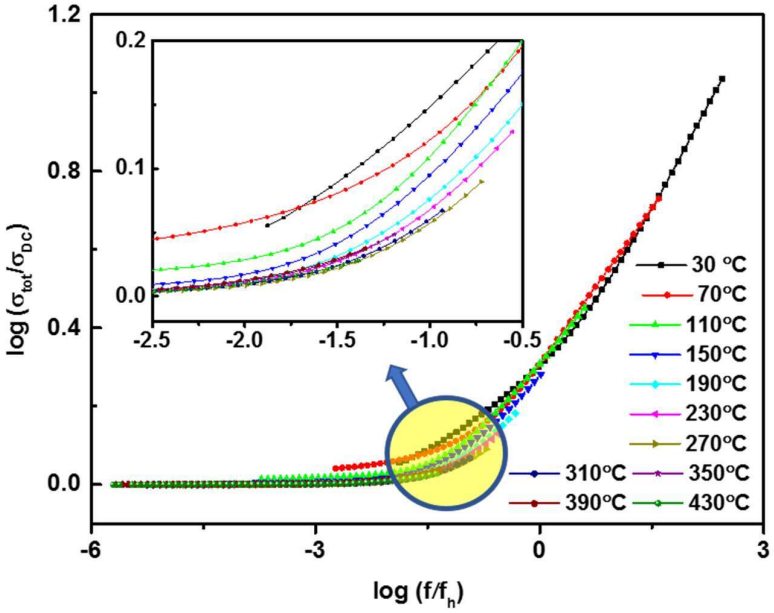


***Figure 3.11. Ghosh scaling for the sample SMQ ($Sr_2MnO_4$).***

The scaling of the conductivity data of sample SMQ at different temperatures has been done using Ghosh scaling approach the results are shown in Fig. 3.11. From the inset of the figure shown in Fig. 3.11, it is seen that above 270 °C, the scaled values collapse into a single master curve, which does not happen below 270 °C. The collapsing of conductivity plots at

different temperatures into a master curve above 270 °C is due to the frequency independent conduction at higher temperatures.

### 3.4.2 Modulus and Impedance Spectroscopic Analysis

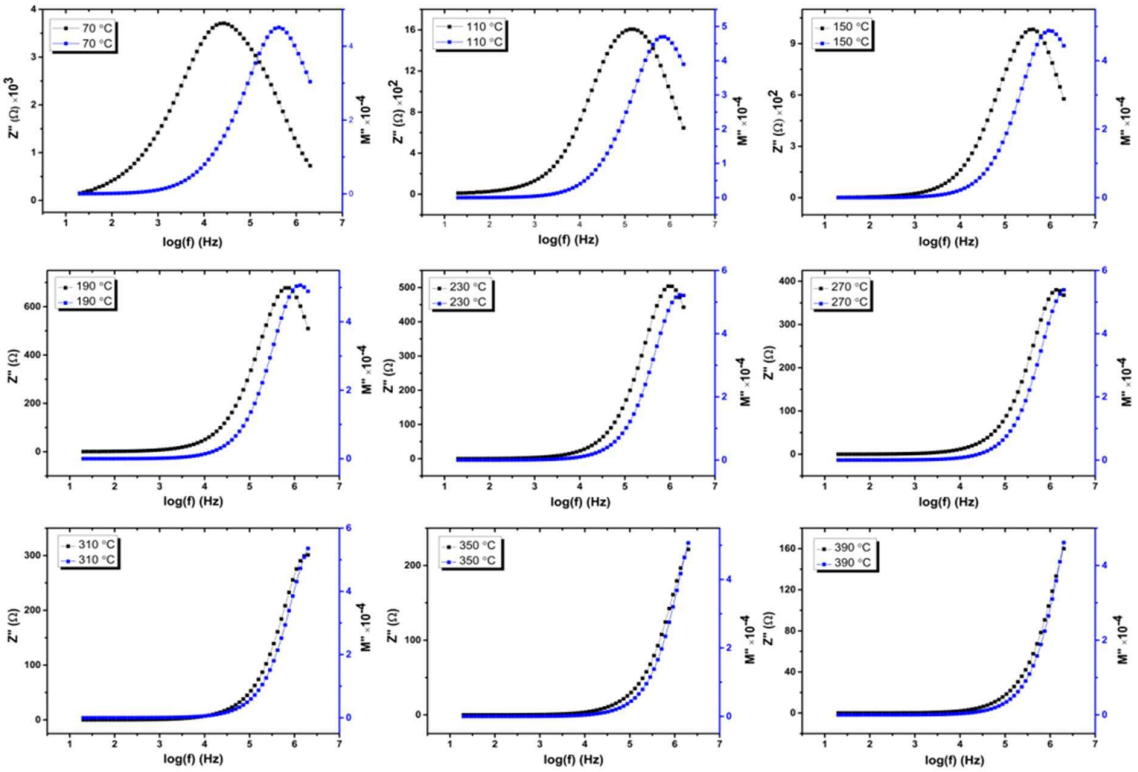


***Figure 3.12. Variation of M'' and Z'' with frequency log (f) at different temperatures for the sample SMQ ($Sr_2MnO_4$).***

The plots of modulus (M*) and impedance (Z*) versus frequency distinguishes the long-range and short-range movement of charge carriers in the conduction and relaxation processes [219]. Hence, for the elucidation of the change in the conduction domain from the short-range to long-range, the imaginary part of impedance (Z'') and modulus (M'') has been plotted against log f as shown in Fig. 3.12. It is noted from Fig. 3.12 that at lower temperatures peak in the Z'' vs. log f plot is broad and asymmetric. As temperature increases, the asymmetric nature of the peak disappears. The asymmetry in the peak in the low-frequency region may be

associated with grain boundaries. Thus, the low-temperature conduction is influenced by the grain boundaries but at higher temperatures the conduction of grains dominates.

The extent of separation in the position of the peaks of M" and Z" with frequency is attributed to the local migration (short-range) of charge carriers whereas superposition of the peaks is due to the long-range migration of charge carriers [220]. From Fig. 3.12 it is observed that at lower temperatures (≤ 300 $^oC$) the peak positions of M" and Z" versus log f plots are different but as the temperature increases, the extent of separation in the peak positions gradually decreases, and finally at 310 $^oC$ both the peaks coincided. The temperature at which peaks coincide is almost the same as the temperature at which the change in the conduction mechanism from short-range to long-range was observed. Thus, the impedance and modulus plots support the change in the domain of the conducting species form short-range to long-range.

## 3.5 Conclusions

The powder and ceramic forms of $Sr_2MnO_4$ were synthesized using the solid-state reaction technique. The calcined powder was sintered at 1500 $^oC$ and then quenched to room temperature. The Rietveld refinement of the XRD profile of the synthesized sample ($Sr_2MnO_4$) confirmed the space group I4/mmm and tetragonal crystal structure. A perfect matching of the XRD patterns of fresh and six-month-old powders–confirmed the long-term stability of the $Sr_2MnO_4$ phase. The FTIR spectrum confirmed the purity of the synthesized sample of $Sr_2MnO_4$. The band-gap of 1.15eV confirmed its semiconductor nature and suitable for solar cell application. The XPS analysis of Mn-2p revealed the existence of $Mn^{3+}$ and $Mn^{4+}$ valence states. The AC conductivity has confirmed the conduction in the sample through polaron tunnelling. The change in conduction mechanism from small polaron to large polaron tunnelling was observed with an increase in the temperature. The nature of Z and M versus log

f plots also confirmed the change in the conduction domain from the short-range (local) to long-range. The conduction can be assumed to be taking place by both polarons and singly ionized oxygen vacancies. These results on the conductivity are the first reports of the AC conduction behavior of $Sr_2MnO_4$. Further theoretical and experimental studies are required to understand the exact mechanism of conduction in $Sr_2MnO_4$.